AIP Journal of Applied Physics

# Room-temperature electro-optic properties of strained SrTiO 3 films grown on DyScO 3

Hongzhou Ma, Jeremy Levy, Michael D. Biegalski, Susan Trolier-McKinstry, and Darrell G. Schlom

Citation: Journal of Applied Physics **105**, 014102 (2009); doi: 10.1063/1.3042238
View online: http://dx.doi.org/10.1063/1.3042238
View Table of Contents: http://scitation.aip.org/content/aip/journal/jap/105/1?ver=pdfcov
Published by the AIP Publishing

# Room-temperature electro-optic properties of strained $SrTiO_3$ films grown on $DyScO_3$

Hongzhou Ma,[1] Jeremy Levy,[1,a)] Michael D. Biegalski,[2] Susan Trolier-McKinstry,[2] and Darrell G. Schlom[3]

[1]*Department of Physics and Astronomy, University of Pittsburgh, Pittsburgh, Pennsylvania 15260, USA*
[2]*Department of Materials Science and Engineering, Pennsylvania State University, University Park, Pennsylvania 16802, USA*
[3]*Department of Materials Science and Engineering, Cornell University, Ithaca, New York 14853-1501, USA*

(Received 27 April 2008; accepted 2 November 2008; published online 6 January 2009)

The electro-optic response of epitaxially strained $SrTiO_3$ grown on bulk $DyScO_3$ substrates is measured as a function of applied in-plane bias (both magnitude and direction) and light polarization. The effective electro-optic coefficients are bias-field dependent. Hysteresis is observed at room temperature, indicative of residual polarity, which is believed to be due to long-lived alignment of nanopolar regions possibly due to defects. A simple model incorporating non-180°-nanoscale domains can account for most of the experimental observations.
 [DOI: 10.1063/1.3042238]

## I. INTRODUCTION

Bulk $SrTiO_3$ is not ferroelectric even at absolute zero temperature. The absence of a true phase transition has been attributed to quantum fluctuations of the soft phonon mode; for this reason $SrTiO_3$ is often referred to as a "quantum paraelectric."[1] The low-temperature state, while nonferroelectric, is nevertheless highly sensitive to dopants or strain.[2–4]

It has recently been demonstrated that highly strained $SrTiO_3$ films on $DyScO_3$ substrates act as relaxor ferroelectrics with permittivity maxima near room temperature.[5] These films are grown on the (110) plane of $DyScO_3$, which has a rectangular surface net with lattice constants that are about 1% larger than that of $SrTiO_3$.[5] This lattice mismatch generates a biaxial state of in-plane tensile strain and causes an orthorhombic structural distortion, resulting in ferroelectricity with an in-plane polarization.[6] Sharp dielectric tuning curves at microwave frequencies are observed with an in-plane dielectric constant as high as 7000 at 10 GHz, dropping by a factor of 5 under modest electric fields ($\sim$70 kV/cm).[5] The "frequency-agile" properties of these materials show potential for tunable microwave devices.

The 25-nm-thick $SrTiO_3$ film was grown on a (110) $DyScO_3$ substrate by reactive molecular-beam epitaxy. The film was grown using molecular beams of strontium, titanium, and a mixture of oxygen (90%) and ozone ($\sim$10%). Growth was performed using a shuttered growth technique[7] at a substrate temperature of 690 °C and an oxidant background pressure of $3\times10^{-5}$ Torr. After growth the film was cooled in the same atmosphere in which it was grown until the substrate temperature was below 200 °C to minimize reduction in the $SrTiO_3$ film. Additional details on the film growth may be found elsewhere.[8,9]

Four-circle x-ray diffraction measurement revealed that the in-plane lattice parameters of the $SrTiO_3$ film were $3.948\pm0.001$ and $3.952\pm0.001$ Å along the orthogonal $[001]_p$ in-plane directions where the substrate has spacings of $3.947\pm0.001$ and $3.952\pm0.001$ Å, respectively (where the $p$ denotes pseudocubic). This corresponds to in-plane strains of 1.1% and 1.2%, respectively, and a 4.5 GPa average residual stress in the film.[10] This indicates that the $SrTiO_3$ film in this study is strained commensurately to the underlying substrate within the $\pm0.001$ Å resolution of our measurements. The out-of-plane lattice parameter of the $SrTiO_3$ film was $3.887\pm0.001$ Å.

The optical properties of bulk and thin film $SrTiO_3$ have been studied extensively.[11–16] Optical probes can help relate structural and dielectric properties and can be used to map polarization dynamics in the gigahertz-terahertz frequency range.[17–20] Moreover, the point group can often be deduced from the symmetry of the electro-optic response.

These measurements on $SrTiO_3/DyScO_3$ reveal a strong field-dependent electro-optic response. The effective electro-optic coefficients are field tunable, similar to the manner in which the microwave-frequency dielectric constant is tunable. There is a small, but measurable, hysteresis in the electro-optic coefficients at room temperature, which contrasts with essentially nonhysteretic polarization—electric field data.[8] We attribute the field dependence to long-lived alignment of nanoscale domains too small to resolve using diffraction-limited optical techniques.

## II. EXPERIMENT PROCEDURE

Confocal scanning optical microscopy[21] (CSOM) is used to measure the local birefringence and electro-optic effect of the 25-nm-thick $SrTiO_3$ film grown on $DyScO_3$ by reactive molecular-beam epitaxy (Fig. 1).[5,8] Linearly polarized light from a laser source (Mira 900, $\lambda=820$ nm, power $=10$ mW) is first spatially filtered by a pinhole and a collimator and then converted into circularly polarized light using a quarter-wave plate. Linearly polarized light of an arbitrary orientation is produced with a second polarizer placed after

a)Electronic mail: jlevy@pitt.edu.

 

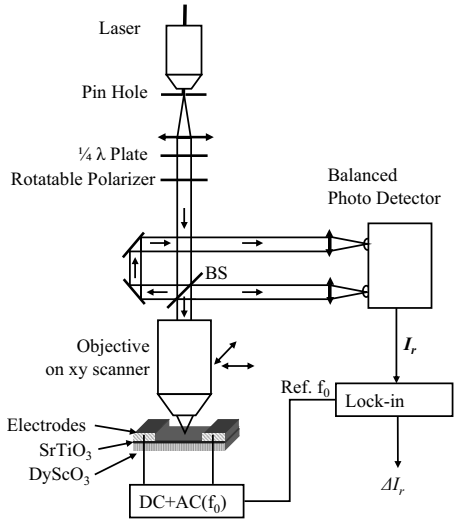


FIG. 1. CSOM setup for electro-optic measurements of $SrTiO_3/DyScO_3$.

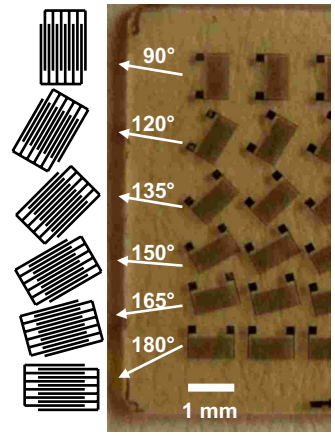


FIG. 2. (Color online) Top view of $SrTiO_3/DyScO_3$ sample with interdigitated electrodes. Six different orientations are available, and five of them were used.

the quarter-wave plate, mounted on a computer-controlled rotation stage. A beam splitter is placed between the pinhole and microscope objective. One beam is directed to a microscope objective (40×, numerical aperture of 0.65) and focused on the sample surface. Light reflected from sample surface is collected by the same objective and its intensity $I_r$ is measured with the signal channel of the balanced photodetector; the other beam is directed to the reference channel.

Ferroelectrics are in general birefringent materials with strong electro-optic effects. To observe the electro-optic response, in-plane electric fields are applied to the sample using interdigitated electrodes. The interdigitated electrodes are aligned so that 90° and 180° patterns are aligned to the edges of the substrate within 0.6° using photolithography. However, the substrate edges are only aligned to the crystallographic $\langle 100\rangle_p$ directions with an error of less than 2°. Thus the angle of the electrode has an error of less than ±3°. Both ac and dc voltages are applied in order to map out the full field-dependent response. In order to measure orientation-dependent effects, the electrodes are oriented at several angles with respect to the crystallographic axes. An applied ac electric field will produce a corresponding modulation of the birefringence and the overall refractive index. The refractive index change is related to the linear electro-optic coefficient, which is a third-rank tensor. The index change also depends on the light polarization and electric field angle. The field-induced reflectivity change is detected optically and isolated using a lock-in amplifier at the frequency of ac driving field. To minimize the noise due to laser power fluctuations and inhomogeneous surface reflectance, the lock-in output signal is normalized by the reflected light intensity $I_r$ to give $\Delta I_r/I_r$.

The ac frequency $f_o$ is set to ~80 kHz, higher than most of the laser noise but within the bandwidth of the balanced photo detector. The electrodes are deposited at several angles (90°, 120°, 135°, 150°, and 180°), as shown in Fig. 2. The gap between electrodes is $d=6$ μm. The objective is mounted on an *xyz* stage, which has both coarse (micrometer-sensitivity) and fine (nanometer-sensitivity) control over all three axes. The *xy* fine control scanning range is $15\times 15$ $\mu m^2$. Reflectivity images are used as a guide to position the focused beam, which is centered between the two interdigitated electrodes. For these experiments the beam position is not scanned. The detected electro-optic signal is recorded as a function of light polarization, dc bias field, and field angle.

Using the normal incidence approximation, the reflectance $r$ can be derived from the Fresnel relation $r=(n-1)^2/(n+1)^2$, and the lock-in signal can be just expressed as its derivative with respect to the electric field $dr/dE$. The normalized reflectance change can be expressed as

$$\frac{1}{r}\frac{dr}{dE}=\frac{4}{n^2-1}\frac{dn}{dE} \tag{1}$$

and the effective electro-optic coefficients is

$$\eta_{\text{eff}}=\frac{d\left(\frac{1}{n^2}\right)}{dE}=-\left(\frac{dr}{r}\right)\frac{n^2-1}{2n^3}\frac{1}{dE}. \tag{2}$$

For $SrTiO_3$, the published value $n=2.34$ was used.[22] The electric field amplitude $dE=E_{\text{ac}}$ is calculated using $E_{\text{ac}}=V_{\text{ac}}/d$, and $dr/r=\Delta I_r/I_r$. Because the optical properties should be the same for light beams with polarization directions that differ by 180°, the data are fitted to a general function

$$f(\theta)=a+b\sin(2\theta)+c\cos(2\theta)+\cdots. \tag{3}$$

Higher order terms such as $\sin(4\theta)$ and $\sin(6\theta)$ are neglected because they are small and unrelated to the linear electro-optic effect, as will be explained below.

## III. RESULTS AND DISCUSSION

The normalized reflectivity $(1/r)(dr/dE)$, proportional to the electro-optic response, is plotted versus linear polarization angle for various values of the static electric field $E_{\text{dc}}$, shown in Fig. 3. In each subplot, the magnitude and direction of the red line represent the magnitude and direction of the applied electric field. Data were collected at a fixed polarization angle for 22 different voltages and 36 different linear polarization angles.

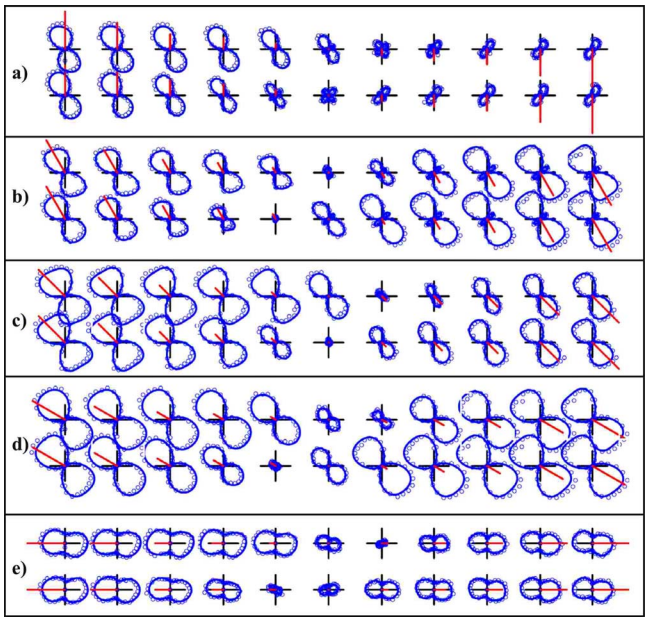


FIG. 3. (Color online) Electro-optic response vs. light polarization plotted as a polar graph. 0° is chosen to be along the vertical axis, with angles increasing in the clockwise direction. Open dots are experimental data. Blue solid lines are fitted according to Eq. (3). Red bars represent the electric field strength and direction. The electric field angles are (a) 180° (or equivalently 0°), (b) 150°, (c) 135°, (d) 120°, and (e) 90°. In each subfigure, data were acquired starting from the top left and proceeding clockwise. The bias voltages are (in volts) −10, −7, −4, −3, −1.5, 0, +1.5, +3, +4, +7, +10, +10, +7, +4, +3, +1.5, 0, −1.5, −3, −4, −7, and −10.

The two-lobe and four-lobe angular distributions present in Fig. 3 are signatures of birefringence. The crystal structure of bulk $SrTiO_3$ is centrosymmetric with no birefringence or linear electro-optic effect. The existence of a linear electro-optic effect demonstrates that this symmetry is broken, at least on a local scale.

Both the magnitude and angular distribution of the electro-optic response depend sensitively on the strength and angle of the bias electric field. For a given field direction, the lobe orientation is not always constant, as can be seen in Figs. 3(a) and 3(e). The effective linear electro-optic coefficients are derived from fits to Eqs. (2) and (3). In Fig. 4, the coefficients in Eq. (3) are plotted versus light polarization and electric field strength. The coefficients show a modest level of hysteresis that is attributed to a long-lived field-induced state. It is important to note that temperature dependent capacitance measurements on similar samples show frequency dispersive dielectric permittivity peaks around 250 K for low frequency electric fields (500 Hz–1 MHz). Moreover, a remanent polarization was shown to develop below room temperature via switching measurements.[8] It is believed that the discrepancy is associated with the difference in length scales probed electrically and optically. The electrical hysteresis measurement probes long-range correlation of the dipole moments at low frequencies. In contrast, optical measurements of relaxor ferroelectrics often show the development of a local polarization at temperatures significantly higher than the permittivity maxima (e.g., the Burn's temperature).[23] Room temperature hysteresis in comparable samples is also observed in second harmonic generation measurement.[24,25] Thus, it is believed that the electro-optic measurements here are associated with local polar regions. Given the uniformity of the CSOM results, the micropolar regions must be quite small (perhaps of the order of 10 nm). Application of an electric field aligns the polarization direction of these nanopolar regions. The existence of some residual hysteresis in the optical measurement is then a consequence of some of these states remaining aligned for longer times (e.g., on the order of hours to days in this work). This could occur either if the activation energy associated with reorientation were large, which should slow down the kinetics of the reorientation, or if the local polar moments interacted with point defects in the films, providing local stabilization. Estimates of the activation energy from Vogel–Fulcher analysis gave a value of 0.05 eV for these films, which is considerably larger than that shown by many lead-based relaxors such as lead magnesium niobate (PMN). It is not clear, at present, which of these two effects dominates in the case of strained $SrTiO_3$ on $DyScO_3$.

From Fig. 4, it is clear that the linear electro-optic response saturates above a certain critical field strength. This could be associated with improved alignment of the nanopolar regions. To try and describe the observed behavior, the linear electro-optic response was modeled under the assumption that the film had *mm*2 point group symmetry[6] using field strengths comparable to the experimental conditions. It was found that the field dependence of the observed electro-optic response cannot be described with a single orientation of the

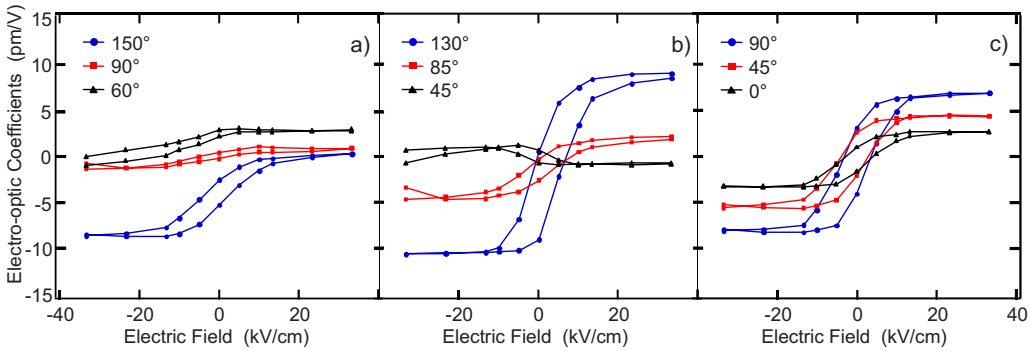


FIG. 4. (Color online) Effective linear electro-optic coefficients vs bias electric field strength at different light polarizations and electric field angles. (a) Electric field at 180°. (b) Electric field at 135°. (c) Electric field at 90°. The legends indicate light polarization. Equation (2) is used to calculate the coefficients.

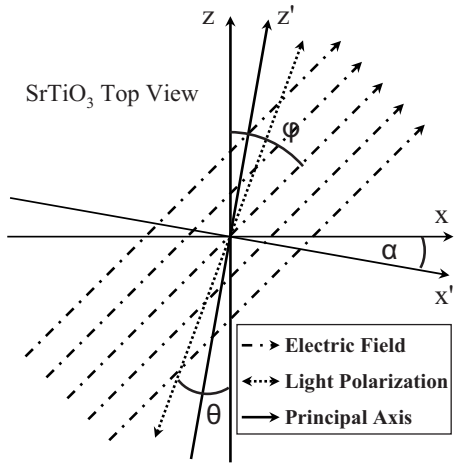


FIG. 5. Definition of various angles. $X$ and $Z$ define the original principal axis of refractive index tensor. $\varphi$ is the electric field angle to $Z$. $X'$ and $Z'$ are the new principal axes of refractive index tensor under external field. $\alpha$ is the angle of the rotation of principal axis.

nanopolar regions. A single domain can only exhibit abrupt changes in electro-optic response due to uniform domain reversal. The model considered allows for four different types of polar directions aligned at 0°, 180°, and ±90° with respect to the possible symmetry axis. This symmetry axis was chosen to be in the direction of 135° of our coordinate systems according to the first principle density-functional calculation for a homogeneously strained film done by Antons *et al.*[6] Therefore, the directions of chosen domains in our coordinate system are +135°, −45°, +225°, and +45°. It should be noted, however, that these directions do not correspond to the observation that the long-range polarization develops first along the longer in-plane axis. We label the relative fractions of those types of domains as $f_1$, $f_2$, $f_3$, and $f_4$ with the normalization constraint $f_1+f_2+f_3+f_4=1$. The coexistence of 90° domains is consistent with the fact that the measured *in-plane* lattice constants are close to each other. Landau free-energy simulations by Li *et al.*[25] also predict the coexistence of 180° and 90° domains. The ratio between 90° domains is fixed because we assume that there is no 90° domain reorientation. In addition to 90° domains, we also assume there are antiparallel ferroelectric domains. The ratio between antiparallel domains depends on the applied electric field. The resulting electro-optic response is plotted in Figs. 6–8 in a fashion similar to Fig. 3. Details of the simulations are given in Sec. IV.

## IV. SIMULATION

The lattice structure of bulk $SrTiO_3$ is centrosymmetric. The substrate produces tensile strain, causing the lattice

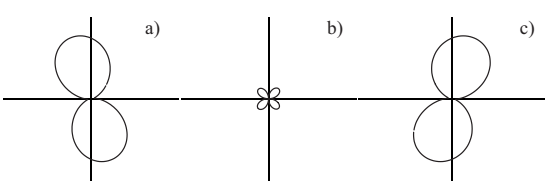


FIG. 6. Simulated electro-optic responses for 180° (or 0°) electric field angle at different ratio between 0°, 180°, +90°, and −90° regions. The fractions of micropolar regions oriented at 0°, 180°, +90°, or −90° $(f_1,f_2,f_3,f_4)$ are given by (a) (0.2, 0.3, 0.5, 0), (b) (0.35, 0.15, 0.35, 0.15), and (c) (0.5, 0, 0.2, 0.3).

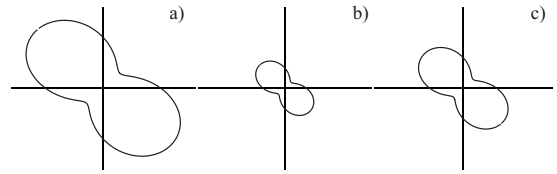


FIG. 7. Simulated electro-optic responses for 135° electric field at different ratio between 0°, 180°, +90°, and −90° domains. The fractions of micropolar regions aligned in a particular orientation are given by (a) (0, 0.65, 0.175, 0.175), (b) (0.195, 0.455, 0.175, 0.175), and (c) (0.52, 0.13, 0.175, 0.175).

structure to become orthorhombic. The relevant form of Pockels tensor (linear electro-optic coefficient) is given by[6,26]

$$r_{ij} = \begin{pmatrix} 0 & 0 & r_{13} \\ 0 & 0 & r_{23} \\ 0 & 0 & r_{33} \\ 0 & r_{42} & 0 \\ r_{51} & 0 & 0 \\ 0 & 0 & 0 \end{pmatrix}. \tag{4}$$

As shown in Fig. 5, the electric field angle $\varphi$ and light polarization $\theta$ are defined with respect to the $z$-axis in the coordinate system along the original (zero electric field) crystal principal axis. In the absence of external electric fields, the impermeability tensor can be diagonalized

$$\frac{1}{n^2} = \eta = \begin{pmatrix} \eta_{11} & 0 & 0 \\ 0 & \eta_{22} & 0 \\ 0 & 0 & \eta_{33} \end{pmatrix}. \tag{5}$$

Under external electric field applied in the $xz$ plane, of which the $y$-component is zero, the new impermeability tensor is given by

$$\frac{1}{n^2} = \eta = \begin{pmatrix} \eta_{11} + r_{13}E_z & 0 & r_{51}E_x \\ 0 & \eta_{22} + r_{23}E_z & 0 \\ r_{51}E_x & 0 & \eta_{33} + r_{33}E_z \end{pmatrix}. \tag{6}$$

The new eigenvalues of the above matrix are

$$\left(\frac{1}{n^2}\right)_{11} = \frac{1}{2}[\eta_{11} + r_{13}E_z + \eta_{33} + r_{33}E_z - \sqrt{(\eta_{11} + r_{13}E_z - \eta_{33} - r_{33}E_z)^2 - 4(r_{51}E_x)^2}], \tag{7}$$

$$\left(\frac{1}{n^2}\right)_{22} = \eta_{22} + r_{23}E_z, \tag{8}$$

$$\left(\frac{1}{n^2}\right)_{11} = \frac{1}{2}[\eta_{11} + r_{13}E_z + \eta_{33} + r_{33}E_z + \sqrt{(\eta_{11} + r_{13}E_z - \eta_{33} - r_{33}E_z)^2 - 4(r_{51}E_x)^2}]. \tag{9}$$

Moreover the corresponding electric field vectors of the light polarization are

$$\left\{1,0,\frac{2r_{51}E_x}{\eta_{11}+r_{13}E_z-\eta_{33}-r_{33}E_z+\sqrt{(\eta_{11}+r_{13}E_z-\eta_{33}-r_{33}E_z)^2-4(r_{51}E_x)^2}}\right\}, \tag{10}$$

$$\{0,1,0\}, \tag{11}$$

$$\left\{1,0,\frac{2r_{51}E_x}{\eta_{11}+r_{13}E_z-\eta_{33}-r_{33}E_z-\sqrt{(\eta_{11}+r_{13}E_z-\eta_{33}-r_{33}E_z)^2-4(r_{51}E_x)^2}}\right\}, \tag{12}$$

where $E_z=E\cos\varphi$ and $E_x=E\sin\varphi$.

The angle of rotation of principal axis is

$$\alpha=\arctan\left\{\frac{2r_{51}E_x}{\eta_{11}+r_{13}E_z-\eta_{33}-r_{33}E_z-\sqrt{(\eta_{11}+r_{13}E_z-\eta_{33}-r_{33}E_z)^2-4(r_{51}E_x)^2}}\right\}. \tag{13}$$

The variation in reflection from the sample surface is the experimentally measured quantity. The reflection ratio is

$$r_x'=\left(\frac{n_x'-1}{n_x'+1}\right)^2,\quad r_z'=\left(\frac{n_z'-1}{n_z'+1}\right)^2, \tag{14}$$

where $n_x'$ and $n_z'$ are the two principal refractive indices in the rotated principal coordinates, and

$$n_x'=\left[\left(\frac{1}{n}\right)^2_{11}\right]^{-1/2},\quad n_z'=\left[\left(\frac{1}{n}\right)^2_{33}\right]^{-1/2}. \tag{15}$$

For arbitrary light polarization $\theta$, relative to $z$ axis, the reflection ratio is

$$r(\theta,E)=r_x'\sin^2(\theta-\alpha)+r_z'\cos^2(\theta-\alpha). \tag{16}$$

This is indeed the form of Eq. (3)

The lock-in detected value, after normalization, is

$$\frac{dI_r}{I_r}=\frac{dr}{r}=\frac{r(\theta,E+dE)-r(\theta,E)}{r(\theta,E)}. \tag{17}$$

All our calculations follow Eqs. (16) and (17). To simulate the experimental result, we used a model of multiple micropolar regions. For all simulations, we set $E=20$ V/(6 $\mu$m), $dE=2$ V/(6 $\mu$m). One of the principal optical axes is chosen to be along 135° to the vertical axis.[6,25] Micropolar regions with their polar axis aligned parallel and antiparallel to this direction are referred to as 0° and 180° regions, respectively. A second principal axis is chosen to be along 45°, and micropolar regions aligned parallel and antiparallel to this direction are referred to as +90° and −90° regions. Several relevant elements in the electro-optic tensor were chosen to be $r_{13}=20$ pm/V, $r_{33}=2$ pm/V, and $r_{51}=10$ pm/V. This provided a reasonable fit to the experimental results. It should be noted, however, that alternative choices for the parameters could give similar results. The dielectric impermeability is set to $(1/n_x^2)=0.17$ and $(1/n_z^2)=0.16$; $n_x$ and $n_z$ are chosen to be close to each other because the effective birefringence for thin films is small.

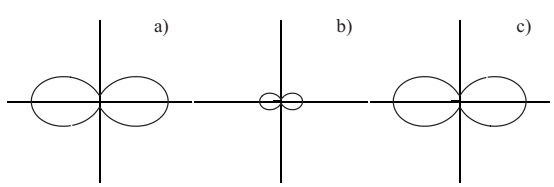


FIG. 8. Simulated electro-optic responses for 90° electric field at different ratio between 0°, 180°, +90°, and −90° domains. The fractions of domains are given by (a) (0.4, 0.1, 0.4, 0.1), (b) (0.3, 0.2, 0.3, 0.2), and (c) (0.1, 0.4, 0.1, 0.4).

From these simulations, we find that the contribution of antiparallel micropolar regions cancels out in the electro-optic response. In Fig. 7, the electric field is 135°, which is perpendicular to the principal axis (or the polar axis of ferroelectric regions) for the +90° and −90° regions and parallel to 0° and 180° regions. The fractions of +90° and −90° regions are fixed at 50/50 ($f_3=f_4=0.175$). In that case, their total contribution to electro-optic effect turns out to be zero. The ratio between 0° and 90° regions is chosen to be 0.65/0.35 to reflect the fact that the electric field is along 0° and breaks the symmetry between micropolar regions aligned along 0° and 90°. The lobe shape and orientation did not change with the ratio between 0° and 180°—only the amplitude changes [as in Fig. 3(c)]. When the ratio between 0° and 180° regions saturates at high bias fields, both the 90° and 180° orientations contribute constructively to the electro-optic effect, consistent with experiment. The electro-optic effect is stronger compared with Figs. 6 and 8 due to the larger fractions of $f_1$ and $f_2$ ($f_1+f_2=0.65$) chosen. This is consistent with experimental results [Fig. 3(c)]. In Fig. 6(a), the electric field direction lies in between the 0° and 90° orientations. All four polar orientations contribute equally (if one neglects the small difference between in-plane lattice constants). By combining them with various weights one can generate the various lobe shapes and orientations seen in Fig. 3(a). However, the relation between the applied field, its history, and the domain fractions is complex and underdetermined by the electro-optic measurements. In Fig. 8, the nanopolar region orientations are in a similar condition as in Fig. 6, but the electric field component in 90° domains is reversed compared with Fig. 6. Again, the fraction is chosen to match observations shown in Fig. 3(e). Simulations with the choice of symmetry axis along 0° are also done. Similar results can be obtained by choosing appropriate $f_1$, $f_2$, $f_3$, and

$f_4$ except that the larger electro-optic responses appear along 0° and 90° in our coordinate system, which are not consistent with the experiment results.

## V. CONCLUSION

The $SrTiO_3$ film grown on $DyScO_3$ substrate appears to be uniform over a $15\times 6$ $\mu m^2$ area (6 $\mu$m is the gap between the electrodes) using the scanning confocal microscope mode shown in Fig. 1. Previous work suggests that localized ferroelectric nanodomains exist,[20,27,28] making it difficult to observe the domain structure using diffraction-limited optics. In this work, a multidomain model for the local polar moments was developed to explain the experimental results. Calculations of the effective electro-optic coefficients, based on this model, agree qualitatively with experimental observations. Higher-resolution probes such as apertureless near-field scanning optical microscopy[20] are required to give more direct evidence for the existence of nanodomains.

## ACKNOWLEDGMENTS

We thank Professor Venkatraman Goplan for several valuable discussions and comments. We gratefully acknowledge the financial support of the National Science Foundation (NSF) under Grant No. DMR-0507146 and the Division of Scientific User Facilities, Basic Energy Sciences, U.S. Department of Energy for funding.

[1] K. A. Muller and H. Burkard, Phys. Rev. B **19**, 3593 (1979).
[2] J. G. Bednorz and K. A. Muller, Phys. Rev. Lett. **52**, 2289 (1984).
[3] M. Itoh, R. Wang, Y. Inaguma, T. Yamaguchi, Y.-J. Shan, and T. Nakamura, Phys. Rev. Lett. **82**, 3540 (1999).
[4] S. Hyun and K. Char, Appl. Phys. Lett. **79**, 254 (2001).
[5] J. H. Haeni, P. Irvin, W. Chang, R. Uecker, P. Reiche, Y. L. Li, S. Choudhury, W. Tian, M. E. Hawley, B. Craigo, A. K. Tagantsev, X. Q. Pan, S. K. Streiffer, L. Q. Chen, S. W. Kirchoefer, J. Levy, and D. G. Schlom, Nature (London) **430**, 758 (2004).
[6] A. Antons, J. B. Neaton, K. M. Rabe, and D. Vanderbilt, Phys. Rev. B **71**, 024102 (2005).
[7] J. H. Haeni, C. D. Theis, and D. G. Schlom, J. Electroceram. **4**, 385 (2000).
[8] M. D. Biegalski, Y. Jia, V. Sherman, R. Uecker, P. Reiche, S. K. Streiffer, D. G. Schlom, and S. Trolier-McKinstry, Appl. Phys. Lett. **88**, 192907 (2006).
[9] M. D. Biegalski, W. Tian, S. Trolier-McKinstry, D. G. Schlom, D. D. Fong, J. A. Eastman, P. H. Fuoss, S. K. Streiffer, M. E. Hawley, R. Uecker, and P. Reiche, J. Appl. Phys.(in press).
[10] E. Poindexter and A. A. Giardini, Phys. Rev. **110**, 1069 (1958). The residual stress was calculated using an average biaxial modulus of 390.6 GPa, calculated from the elastic constants of strontium titanate from this reference.
[11] E. Courtens, Phys. Rev. Lett. **29**, 1380 (1972).
[12] J. Petzelt, T. Ostapchuk, I. Gregora, I. Rychetsky, S. Hoffmann-Eifert, A. V. Pronin, Y. Yuzyuk, B. P. Gorshunov, S. Kamba, V. Bovtun, J. Pokorny, M. Savinov, V. Porokhonskyy, D. Rafaja, P. Vanek, A. Almeida, M. R. Chaves, A. A. Volkov, M. Dressel, and R. Waser, Phys. Rev. B **64**, 184111 (2001).
[13] H. Hasebe, Y. Tsujimi, R. Wang, M. Itoh, and T. Yagi, Phys. Rev. B **68**, 014109 (2003).
[14] O. Tikhomirov, H. Jiang, and J. Levy, Phys. Rev. Lett. **89**, 147601 (2002).
[15] M. Yamaguchi, T. Yagi, R. Wang, and M. Itoh, Phys. Rev. B **63**, 172102 (2001).
[16] R. S. K. S. Gupta, J. Raman Spectrosc. **32**, 885 (2001).
[17] A. A. Sirenko, C. Bernhard, A. Golnik, A. M. Clark, J. H. Hao, W. D. Si, and X. X. Xi, Nature (London) **404**, 373 (2000).
[18] P. Kuzel, F. Kadlec, H. Nemec, R. Ott, E. Hollmann, and N. Klein, Appl. Phys. Lett. **88**, 102901 (2006).
[19] M. Misra, K. Kotani, I. Kawayama, H. Murakami, and M. Tonouchi, Appl. Phys. Lett. **87**, 182909 (2005).
[20] H. Ma and J. Levy, Nano Lett. **6**, 341 (2006).
[21] C. Hubert, J. Levy, A. C. Carter, W. Chang, S. W. Kiechoefer, J. S. Horwitz, and D. B. Chrisey, Appl. Phys. Lett. **71**, 3353 (1997).
[22] *Handbook of Optics* (McGraw-Hill, New York, 1995), Vol. II.
[23] G. Burns and F. H. Dacol, Phys. Rev. B **28**, 2527 (1983).
[24] A. Vasudevarao, A. Kumar, L. Tian, J. H. Haeni, Y. L. Li, C.-J. Eklund, Q. X. Jia, R. Uecker, P. Reiche, K. M. Rabe, L. Q. Chen, D. G. Schlom, and V. Gopalan, Phys. Rev. Lett. **97**, 257602 (2006).
[25] Y. L. Li, S. Choudhury, J. H. Haeni, M. D. Biegalski, A. Vasudevarao, A. Sharan, H. Z. Ma, J. Levy, V. Gopalan, S. Trolier-McKinstry, D. G. Schlom, Q. X. Jia, and L. Q. Chen, Phys. Rev. B **73**, 184112 (2006).
[26] D. D. Nolte, *Photorefractive Effect and Materials* (Kluwer Academic, Boston, 1995).
[27] F. Xu, S. Trolier-McKinstry, W. Ren, B. M. Xu, Z. L. Xie, and K. J. Hemker, J. Appl. Phys. **89**, 1336 (2001).
[28] C. Hubert, J. Levy, T. V. Rivkin, C. Carlson, P. A. Parilla, J. D. Perkins, and D. S. Ginley, Appl. Phys. Lett. **79**, 2058 (2001).